

Interaction mechanism between edge dislocations and asymmetrical tilt grain boundaries investigated via quasicontinuum simulations

T. Shimokawa, T. Kinari, and S. Shintaku

Division of Mechanical Science and Engineering, Graduate School of Natural Science and Technology, Kanazawa University, Kakuma-machi, Kanazawa, Ishikawa 920-1192, Japan

(Received 28 August 2006; revised manuscript received 28 December 2006; published 23 April 2007)

The interactions between edge dislocations and grain boundaries—dislocation pileup, dislocation absorption, and dislocation transmission—are studied by performing quasicontinuum simulations. The $\langle 112 \rangle$ asymmetrical tilt grain boundaries with different misorientation angles are used. The atomic configurations and stress fields of equilibrium and nonequilibrium asymmetrical grain boundaries are investigated in detail by comparison with analytical models. The influence of the grain boundary structure on the stress concentration due to dislocation pileup and the accommodation of extrinsic dislocations in the grain boundaries are also examined by using low- and high-angle grain boundaries. The critical forces on the dislocation in small-angle tilt grain boundaries for it to eject from the boundaries are evaluated by atomic simulations, and the results are compared with dislocation theory. It is also found that the rearrangement of the grain boundary dislocations with local grain boundary sliding in the local region, where the extrinsic dislocation is absorbed, is the characteristic accommodation mechanism of low-angle asymmetrical grain boundaries. The effects of the interaction between dislocations and grain boundaries on the mechanical properties of coarse-grained metals with dislocation sources in their grain and on those of nanocrystalline metals without sources in their grain are also discussed.

DOI: [10.1103/PhysRevB.75.144108](https://doi.org/10.1103/PhysRevB.75.144108)

PACS number(s): 61.72.Yx, 62.20.Fe, 02.70.Ns

I. INTRODUCTIONS

Plastic deformation of polycrystalline metals at non-elevated temperatures occurs mainly due to the motion of dislocations. Therefore, the macroscopic mechanical properties of these metals are strongly governed by the presence of obstacles in the path of dislocation motion. The strongest obstacle must be a grain boundary—the interface between two crystal grains with different crystal orientations. In coarse-grained metals, the influence of the grain boundary on the mechanical properties can be described by the Hall-Petch relationship:^{1,2} a plot of the yield stress σ_y against $d^{-1/2}$ produces a constant slope k_y . Generally, the Hall-Petch slope k_y could be a material-dependent value; however, it has been reported that k_y varies in the same material due to differences in the grain boundary structure.³ On the other hand, as the grain size decreases to 100 nm, the plot of σ_y against $d^{-1/2}$ deviates from the original Hall-Petch slope, and the deformation flow stress exhibits a strong dependence on the temperature and strain rate.^{4,5} In such nanocrystalline metals,⁶ it is difficult to maintain dislocation sources and form dislocation cells or subgrains in nanograins; therefore, it can be presumed that the grain boundary becomes an important dislocation source and sink. Consequently, in order to understand the mechanical properties of polycrystalline metals, it is very important to elucidate the phenomenon of the interaction between dislocations and the grain boundary—dislocation pileup, dislocation absorption, and dislocation transmission.

A large number of investigative studies have been performed on the interaction between dislocations and the grain boundary by using analytical models^{7,8} for the accommodation of extrinsic dislocations in the grain boundary and transmission electron microscopy observations⁹ of actual materials. However, these methods are inadequate for determining these interactions in detail. Previous studies either do not

consider the influence of the detailed grain boundary structure on the extrinsic dislocations in the delocalization¹⁰ and dissociation¹¹ models or treat only the grain boundaries expressed by the grain boundary dislocations in the incorporation model.¹² The latter type of studies could not obtain a series of high-resolution images on the atomic scale during the interactions between dislocations and the grain boundary or the accommodation of the extrinsic dislocations. Atomic simulation is one of the powerful tools that can overcome the shortcomings of the above-mentioned studies. This is because it can be used to directly treat the individual lattice defects in a hypothetical material which are expressed by an atomic potential. Accordingly, the relationship between the internal structure and the mechanical properties of a material can be explicitly examined by performing atomic simulations. The effectiveness of this method has been confirmed by important studies on the deformation mechanism and mechanical properties of nanocrystalline metals that contain a large number of lattice defects.^{13–16} The relationship between dislocations and the grain boundary has also been studied by performing atomic simulations.^{17–20} However, it is noteworthy that an isolated dislocation exhibits long-range stress fields, i.e., the stresses are inversely proportional to the distance from the dislocation core.²¹ Hence, we require a large-scale atomic model to circumvent the artificial effect due to the boundary condition on the dislocation motion.

The quasicontinuum (QC) method, first proposed by Tadmore *et al.*,²² is a concurrent multiscale method that couples atomistic and continuum descriptions. Therefore, this method can efficiently simulate the interaction between defect structures by expressing regions distant from the lattice defects as continuum fields.^{23–25} Further, the QC method has an advantage in that the anisotropic elasticity and nonlinear elastic properties can be expressed equivalently in different description regions. This is because the constitutive rule in the con-

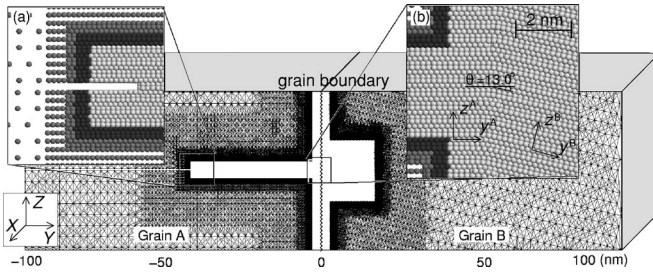


FIG. 1. Atomic configuration of the analysis model comprising two grains—*A* and *B*. The misorientation angle θ is set to 13.0° . Magnified images in the vicinity of the (a) crack tip and (b) grain boundary. Light, medium, and dark gray atoms represent “nonlocal,” “local,” and “quasinonlocal” atoms, respectively. Dimensions along the *X*, *Y*, and *Z* directions are approximately 24, 55, and 200 nm, respectively.

tinuum description is expressed by using the same atomic potential as that adopted in the atomistic description. The problem with the QC method lies in the manner in which the seamless coupling between the atomistic and continuum regions can be expressed; this is because nonphysical forces appear at the interface of the two regions due to the different descriptions used to calculate the potential energy for each region.²⁶ However, we have determined a method to eliminate the nonphysical forces in the case of homogeneous strain fields by introducing a buffer layer between the two regions.²⁷

When an edge dislocation is absorbed by a grain boundary whose normal direction is perpendicular to the dislocation line, a geometrical misfit that corresponds to the magnitude of the Burgers vector of the edge dislocation is necessarily generated; consequently, a volume change occurs toward the grain boundary plane. In the case of screw dislocation, however, this type of volume change does not occur.¹⁹ Hence, it would be very interesting to investigate the accommodation mechanism of incoming edge dislocations in grain boundaries. In this study, we investigate the detailed interaction mechanism between edge dislocations and asymmetrical tilt grain boundaries by using our improved QC simulations. We use four $\langle 112 \rangle$ asymmetrical tilt grain boundaries with different misorientation angles in order to investigate the influence of the asymmetrical grain boundary structures on the accommodation of *extrinsic* grain boundary dislocations (EGBDs). We also compare the results obtained in the atomic simulations, e.g., the grain boundary structures and the critical force on the dislocation in the grain boundary for it to eject from the boundary, with the dislocation theory.²¹ Finally, on the basis of our results, we discuss the effect of the grain boundary structure on the unique mechanical properties of nanocrystalline metals.

II. METHODOLOGY

A. Analysis models

Figure 1 shows the schematic of the analysis model. The embedded atom method for aluminum developed by Mishin *et al.*²⁸ is used. The fault energies estimated using the inter-

atomic potentials are the same as the energies obtained from experimental data and *ab initio* calculations, e.g., the stacking fault energy. The analysis model comprises two crystal grains—*A* and *B*—and a crack is introduced as the dislocation source in grain *A*. The region near the dislocation slip plane in grain *A* and that near the grain boundary between grains *A* and *B* exhibit full atomistic resolution, i.e., they contain nonlocal atoms,²⁶ as indicated by the white regions in Fig. 1. On the other hand, the regions distant from the slip plane or the grain boundary are divided into finite elements. Therefore, the mechanics of atoms in an element of this region should conform to the positions of the node atoms, i.e., local atoms²⁶ should be present. In order to eliminate the nonphysical forces that appear at the coupling interface, we introduce buffer layers, i.e., quasi nonlocal atoms,²⁷ between the atomistic and continuum regions. The light, medium, and dark gray atoms in the enlarged pictures in Fig. 1 represent the nonlocal, local, and quasinonlocal atoms, respectively.

In order to generate edge dislocations from the crack in grain *A* under shear deformation γ_{ZY} , the crystal orientations along the x^A , y^A , and z^A directions of grain *A* are set to $[\bar{1}\bar{1}2]$, $[\bar{1}10]$, and $[111]$, respectively. The crystal orientation along the x^B direction of grain *B* is also set to $[\bar{1}\bar{1}2]$. Therefore, the grain boundary structure in this model is controlled by the rotational angle θ around the *X* direction. Periodic boundary conditions are adopted along the *X* and *Z* directions; hence, the grain boundaries have infinite structural periodicity and belong to the family of the $\langle 112 \rangle$ asymmetrical tilt grain boundary. Four analysis models with different misorientation angles— 13° , 29.5° , 63.0° , and 89.3° —are prepared. These angles are carefully selected in order to ensure that almost no residual strain ε_{ZZ}^R remains in grains *A* and *B*; $\varepsilon_{ZZ}^R < 0.04\%$. These models are numbered from 1 to 4; for example, “model 1” denotes the first model.

For each model, the dimensions along the *X*, *Y*, and *Z* directions are approximately 24, 200, and 55 nm, respectively. The distance between the crack tip and the grain boundary is approximately 40 nm. The sum of the nonlocal, local, and quasinonlocal atoms in each model is approximately 1.5×10^6 . If the analysis model uses only nonlocal atoms, the total number of atoms is approximately 16×10^6 . Consequently, the number of degrees of freedom in this QC model is one-tenth that in a full atomistic model.

B. Analysis conditions

We apply the Delaunay triangulation to the finite element mesh. In order to simulate the interactions between the incoming dislocations and the tilt grain boundaries, the shear strain increment $\Delta\gamma_{ZY}$ is repeatedly applied to the analysis models. The energy of the analysis model for each $\Delta\gamma_{ZY}$ is minimized by the conjugate gradient method; no thermally activated process is considered in this study. The value of $\Delta\gamma_{ZY}$ is 0.002. Under the shear deformation, the *Z*-directional displacement of the surface nodes along the *Y* direction is fixed. The local atomic structure is distinguished by using the common neighbor analysis method.²⁹

III. RESULTS

First, we investigate the effect of the coupling interfaces in the QC method with the quasinonlocal atoms on the inho-

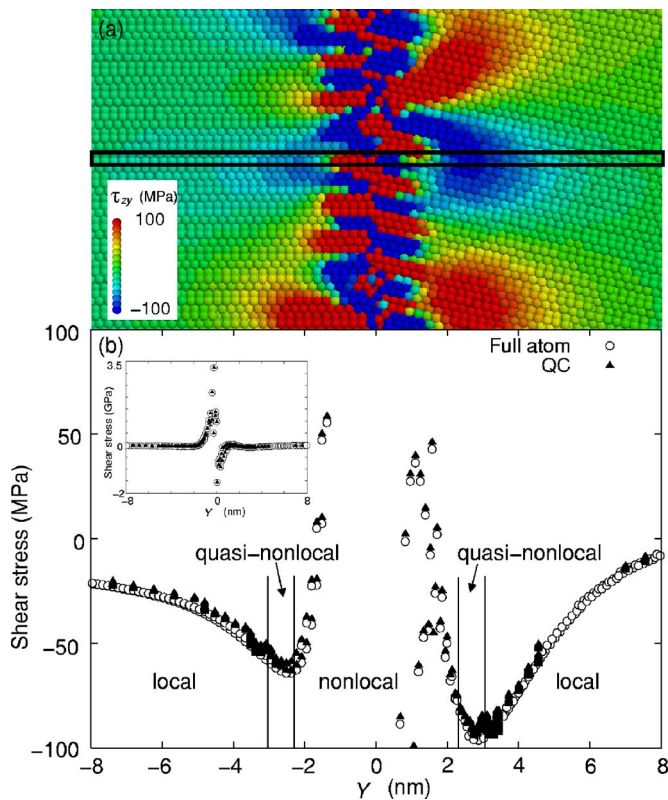


FIG. 2. (Color online) Distributions of the shear stress τ_{ZY} in the vicinity of the grain boundary expressed by the full atomistic resolution and the quasicontinuum methods in model 1. (a) Atomic configurations in the full atomistic model, and (b) shear stress in the square region shown in Fig. 2(a).

homogeneous strain fields. Figure 2(a) shows the shear stress τ_{ZY} around the grain boundary in model 1 expressed by full atomistic resolution. Localized inhomogeneous stress fields can be observed around the grain boundary. Figure 2(b) shows the distributions of the shear stress τ_{ZY} in the square region shown in Fig. 2(a) in the full atomistic model and the QC model, respectively. The inset corresponds to the case where the full range of the shear stress is applied, and it is evident that almost the same shear stress distributions can be obtained in the QC model. The four solid lines in Fig. 2(b) represent the coupling interfaces between nonlocal/quasinonlocal and quasinonlocal/local regions, respectively. The remarkable gaps in the shear stress at the coupling interface cannot be confirmed. The differences between the shear stress around the grain boundary and the grain boundary energy in the QC model and the full atomistic model are approximately 4 MPa and less than 0.5% of the energy of the full atomistic model, respectively. Consequently, we can conclude that the effect of the coupling interface in this QC method on inhomogeneous strain fields is very small, and we can perform QC simulations without introducing a fatal error into the results obtained in this study.

A. Asymmetrical tilt grain boundary structures

Figure 3 shows the atomic configurations and arrangements of the grain boundary dislocations in the vicinity of

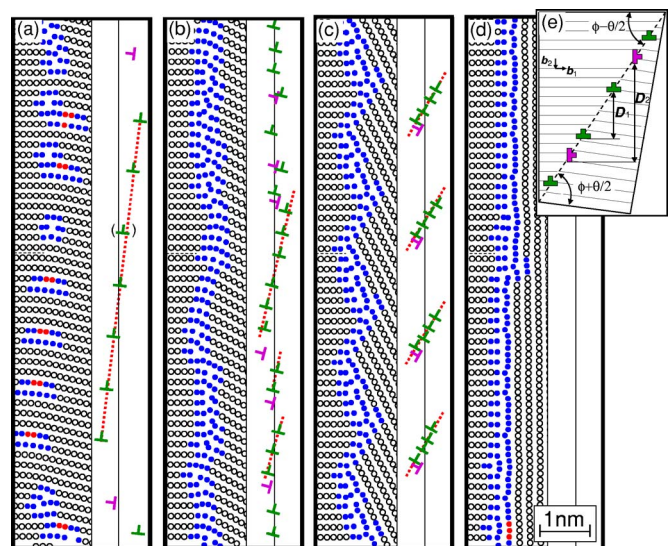


FIG. 3. (Color online) Asymmetrical tilt grain boundary structures of two (112) atomic planes in different analysis models. (a) Model 1, $\theta=13.0^\circ$; (b) model 2, $\theta=29.5^\circ$; (c) model 3, $\theta=63.0^\circ$; and (d) model 4, $\theta=89.3^\circ$. Open, red (dark gray), and blue (black) circles represent atoms in the local fcc, hcp, and defect environments, respectively. Two sets of grain boundary dislocations shown in green (dark gray) and magenta (light gray) can be observed in the low-angle tilt grain boundaries. Solid lines represent the actual asymmetrical grain boundary planes, and red (dark gray) broken lines represent the symmetrical grain boundary planes. Black thin broken lines in atomic configurations indicate the slip planes of the incoming dislocations from the crack tip. (e) Schematic of the tilt grain boundary composed of two sets of uniformly spaced edge dislocations D_1 and D_2 .

the grain boundaries in the relaxation state. The white, red (dark gray), and blue (black) circles represent the atoms in the local fcc, hcp, and defect structures, respectively. The grain boundary structures in models 1 and 2 are completely expressed, while the structure in model 3 is partially expressed by two sets of edge dislocations, as shown in Figs. 3(a)–3(c). On the other hand, as shown in Fig. 3(d), it is difficult to depict the structure in the case of model 4, which has a high angle, by dislocations. It should be noted that the relaxed grain boundary structures in this study are obtained by energy minimization, i.e., at $T=0$ K. Hence, it is possible that the structures descend to a metastable state that is distant from the state of the thermal equilibrium grain boundary. As will be mentioned subsequently, the grain boundary energies in this study are approximately 5–7% higher than those of the grain boundaries for which the atomic configurations at 0 K are obtained after relaxation at a finite temperature $T=300$ K with smaller models by molecular dynamics simulations. Moreover, the arrangements of grain boundary dislocations in this study and obtained after relaxation at the finite temperature do not show remarkable differences. Accordingly, it could be reasonable to study the mechanism of interaction between dislocations and grain boundaries by using the relaxed grain boundary structures obtained by the QC simulations.

Analytically, two sets of uniformly spaced edge dislocations are required to construct an asymmetrical low-angle tilt

TABLE I. Asymmetrical grain boundary properties. The values in parentheses are analytically estimated.

	Model 1	Model 2	Model 3	Model 4
θ	13.0°	29.5°	63.0°	89.3°
$\phi-90^\circ$	7° (6.5°)	14° (15°)	32° (31.5°)	
D_1 (nm)	1.25 (1.27)	0.59 (0.57)	(0.31)	
D_2 (nm)	10.05 (9.07)	1.82 (1.78)	(0.41)	
E^{GB} (mJ/m ²)	431	552	427	476
V^{GB} (nm)	0.028	0.035	0.035	0.042

grain boundary,³⁰ as shown in Fig. 3(e). The Burgers vectors of these grain boundary dislocations— \mathbf{b}_1 and \mathbf{b}_2 —are perpendicular to each other. The dislocations that accommodate the geometrical misfits between two grains with different crystal orientations are referred to as *intrinsic* grain boundary dislocations (IGBDs). A grain boundary that comprises only IGBDs has no long-range stress fields. The spacings along the boundary of two dislocation sets are calculated by the following equations:³⁰

$$D_1 = \frac{b_1}{\theta \sin \phi}, \quad D_2 = \frac{b_2}{\theta \cos \phi}. \quad (1)$$

In this study, the magnitudes of \mathbf{b}_1 and \mathbf{b}_2 in the $\langle 112 \rangle$ asymmetrical tilt grain boundaries are $\sqrt{2}/2a_0$ and $\sqrt{3}/3a_0$, respectively. The average spacing between the two dislocation sets in the atomic structures and the analytical spacing calculated by Eq. (1) are listed in Table I. The analytical values are shown in parentheses. In the case of the low-angle grain boundary, D_1 and D_2 obtained by using the atomic and analytical models have almost the same values; therefore, the grain boundaries in our atomic model comprise only IGBDs.

Figure 4(a) shows the distribution of the shear stress τ_{ZY} in the vicinity of the grain boundary in model 2; no long-range stress fields are observed. On the other hand, in the case of the grain boundary with an extra edge dislocation with \mathbf{b}_1 , the EGBD and long-range stress fields can be observed, as shown in Fig. 4(b). No external force is applied to

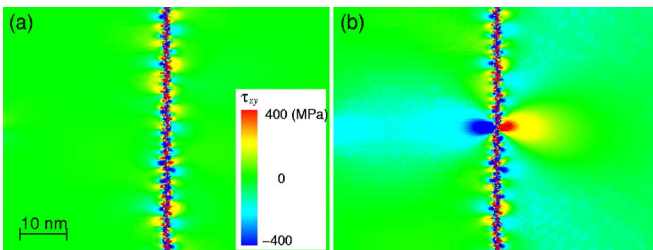


FIG. 4. (Color online) Distributions of shear stress τ_{ZY} around the tilt grain boundary in model 2 under no external applied stress. (a) The tilt grain boundary is composed of only IGBDs, as shown in Fig. 3(b)—equilibrium grain boundary. (b) Tilt grain boundary with the same misorientation angle of model 2 but containing an EGBD—nonequilibrium grain boundary. The detailed atomic configuration of the grain boundary with one EGBD is almost the same as that shown in Fig. 9(b).

either model. Hence, it can be considered that the former and latter images correspond to the equilibrium and nonequilibrium grain boundaries, respectively. Most grain boundaries in atomic simulations, e.g., the initial grain boundary structure in nanocrystalline metals prepared by using the Voronoi construction to determine individual grain spaces,^{16,31} can be estimated to be the equilibrium grain boundary. However, the actual grain boundary in nanocrystalline metals produced by severe plastic deformations with insufficient annealing could contain a large number of EGBDs.³² Therefore, we should carefully treat the grain boundary structure in the atomic simulation to investigate the distinctive mechanical properties of nanocrystalline metals.^{4,5}

The values of $\phi-90^\circ$ in Table I represent the deviation angle of the actual grain boundary plane from the symmetrical grain boundary plane. The analytical deviation angles in models 1, 2, and 3 are 6.5°, 15°, and 31.5°, respectively. On the other hand, as shown in Fig. 3, edge dislocations (green lines) are arranged along the symmetrical plane (red broken lines), and the deviation angles in the atomic models are 7°, 14°, and 32°, which are very close to the analytical values. Hence, the edge dislocations along the symmetrical plane that corresponds to the energetic stable sites of the edge dislocation array primarily accommodate the misfit by different crystal orientations of grains *A* and *B*. In this study, these dislocations are referred to as *primary* IGBDs. On the other hand, the edge dislocations shown in magenta (light gray) accommodate the gaps between the actual and symmetrical grain boundary planes. We refer to these dislocations as *secondary* IGBDs and they can also be broadly referred to as displacement shift complete³³ (DSC) dislocations.

The grain boundary energies E^{GB} and grain boundary volumes V^{GB} for each model are also listed in Table I. In this study, the grain boundary volume is defined as $\sum_{i=1}^N (V_i - V_0)/A^{\text{GB}}$. Here, V_i represents the atomic free volume of the i th atom in the region containing the grain boundary, V_0 , the atomic free volume in the fcc structure; and A^{GB} , the grain boundary area. Consequently, the grain boundary volume corresponds to the values of the thickness increment at the interface due to the existence of the grain boundary. It can be observed that V^{GB} increases with θ ; however, E^{GB} does not exhibit a clear dependence on θ . In the $\langle 112 \rangle$ tilt grain boundary, the $\Sigma 11$ grain boundary appears when $\theta=63.96^\circ$. Hence, the symmetrical structure in the grain boundary in model 3 is in a stable state, $\Sigma 11$, and the value of E^{GB} in model 3 is the lowest among the models investigated in this study.

B. Dislocation–grain boundary interactions

Table II lists the number of dislocations in the pileup and those absorbed by the grain boundary under shear deformation. The arrows on the right represent the dislocation transmission into grain *B*. Model 1' will be discussed in the next section. Figures 5(a)–5(d) show the final atomic configurations in each model under shear deformation in this study. Figures 5(e)–5(h) show a series of atomic configurations in model 2 under γ_{ZY} . In order to help understand the defect structures, the atoms in the local fcc structure are not shown

TABLE II. Number of dislocations in the pileup (left) and dislocations absorbed by the grain boundary (right). Right arrows represent the dislocation transition to the neighboring grain.

γ_{ZY}	0.012	0.014	0.016	0.018	0.020	0.022	0.024	0.026	0.028	0.030	0.032	0.034	0.036	0.038
Model 1	0,1	0,1	1,1	2,1	3,1	3,1	3,1→							
Model 1'	0,1	0,1	1,1	1,1	1,1	1,1	1,1	1,1	1,1	1,1	1,1	1,1	1,1	1,1
Model 2	0,1	1,1	1,1	2,1	3,1	3,1	4,1	4,1	4,2	5,2	5,2	5,2→		
Model 3	0,1	0,1	1,1	2,1	3,1	3,1	4,1	3,2	4,2	5,2	5,2	6,2→		
Model 4	0,1	0,1	1,1	2,1	3,1	3,1	4,1	5,1	4,2	5,2	5,2	6,2	7,2	

in Fig. 5. The atoms in the local hcp and defect structures are shown in brown (dark gray) and gray (light gray), respectively. The defect atoms in the grain boundaries are shown as transparent circles. The dislocations from the crack tip are numbered in order. The distributions of τ_{ZY} are also shown in each background. The black lines show the coupling interface between the atomistic and continuum regions in grain *B*, and the seamless distribution of τ_{ZY} can be observed.

The stress concentration in front of the crack tip increases with γ_{ZY} , as shown in Fig. 5(e). Further, it is evident that the first dislocations originate from the crack tip when γ_{ZY} reaches 0.012 in all the models, as shown in Table II. All first dislocations are absorbed by the grain boundaries. The number of dislocations in the pileup increases with γ_{ZY} . Further, the stress concentration ahead of the dislocation pileup can be observed as shown in Figs. 5(f)–5(h). Finally, the dislo-

cation transmission occurs in model 1 when γ_{ZY} reaches 0.024 and the grain boundary absorbs another incoming dislocation, as shown in Fig. 5(a). Similarly, the dislocation transmission occurs in model 2 when γ_{ZY} reaches 0.034 and two incoming dislocations are absorbed by the grain boundary, as shown in Fig. 5(b). In the cases of models 3 and 4, the major operative slip system in the fcc structure cannot be activated in grain *B*; the $\{311\}\langle 110\rangle$ slip system is present in grain *B* in model 3. It should be noted that a geometrical restriction is imposed along the direction of the dislocation line due to the *X*-directional periodic boundary condition.

C. Stress concentration due to dislocation pileup

In order to investigate the influence of dislocation pileup on the stress concentration, Fig. 6(a) shows a plot of the macroscopic shear stress τ_{ZY}^I against γ_{ZY} in region I: $-30 \leq Y \leq 50$ nm (shown in inset). Figure 6(b) shows a plot of the microscopic shear stress τ_{ZY}^{II} against γ_{ZY} in region II: $0 \leq Y \leq 5$ nm and $-2.5 \leq Z \leq 2.5$ nm. As shown in Fig. 6(a), in all the models, τ_{ZY}^I increases linearly with γ_{ZY} before the generation of the first dislocation. The slopes are almost the same for each model because the anisotropy factor— $2C_{44}/(C_{11}-C_{12})$ —is very close to the one (approximately 1.25) for the adopted atomic potential. The plastic deformation begins to be dominant after the first dislocations originate from the crack tip; the slopes of τ_{ZY}^I decrease in comparison with the slope under elastic deformation. The microscopic shear stress τ_{ZY}^{II} in region II in front of the dislocation pileup is in good agreement with τ_{ZY}^I until $\gamma_{ZY} = 0.012$. However, a drastic increase in τ_{ZY}^{II} can be observed in all the models when the first dislocations are absorbed by the grain boundaries. It is also clearly observed that the increment rate of τ_{ZY}^{II} is larger than that of τ_{ZY}^I due to the dislocation pileup, and the increment rate of τ_{ZY}^{II} does not exhibit a strong dependence on the grain boundary structures.

In order to investigate the influence of the number of dislocations in the pileup on the stress concentration, the atomic displacements in the crack tip are fixed to control the number of dislocations originating from the crack tip during energy minimization after $\gamma_{ZY} = 0.016$ in model 1. We refer to the simulation performed under this condition as model 1'. In this model, the third dislocation cannot originate from the crack tip under a large shear deformation, as shown in Table II; one dislocation is present in the pileup and another is absorbed by the grain boundary. Hence, in this model, the elastic deformation is once again dominant after $\gamma_{ZY} = 0.016$;

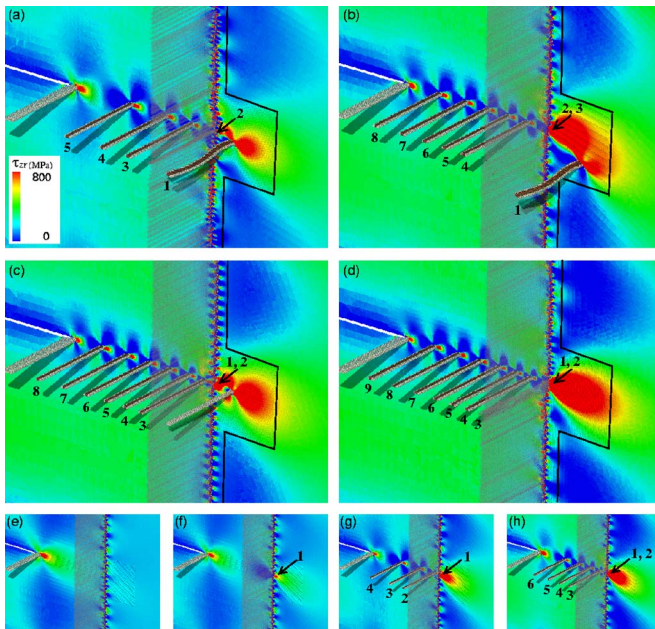


FIG. 5. (Color online) Interactions between lattice edge dislocations from the crack tip and asymmetrical tilt grain boundaries under shear deformation. (a) Model 1, $\theta = 13.0^\circ$, $\gamma_{ZY} = 0.024$; (b) model 2, $\theta = 29.5^\circ$, $\gamma_{ZY} = 0.034$; (c) model 3, $\theta = 63.0^\circ$, $\gamma_{ZY} = 0.034$; and (d) model 4, $\theta = 89.3^\circ$, $\gamma_{ZY} = 0.036$. (e)–(h) Model 2, $\gamma_{ZY} = 0.010, 0.012, 0.020, \text{ and } 0.028$, respectively. Atoms in the local hcp and defect environments are shown in brown (dark gray) and gray (light gray), respectively. Defect atoms in the grain boundary regions are shown as transparent atoms.

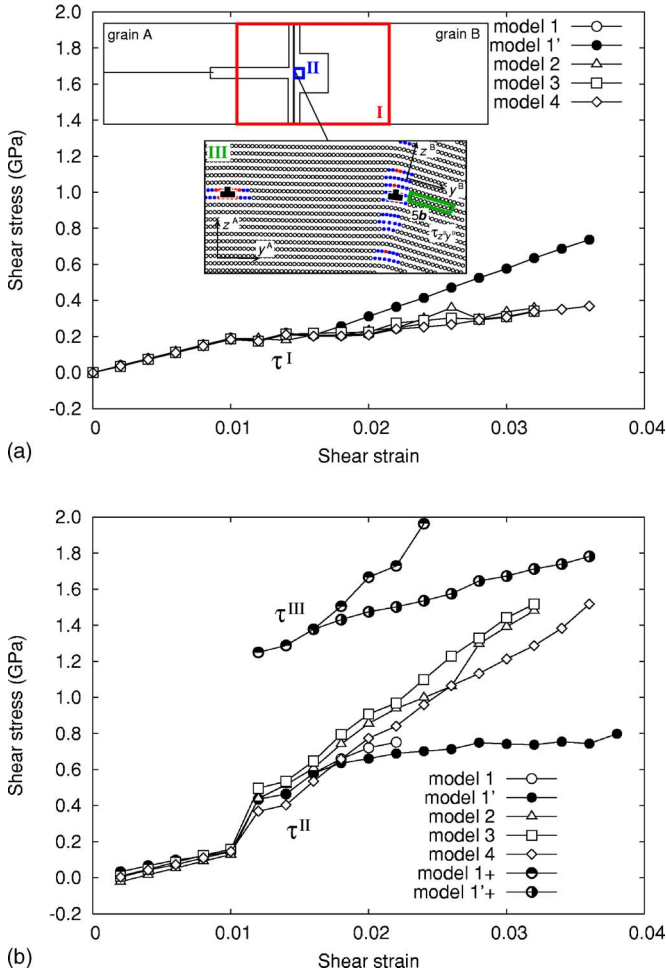


FIG. 6. (Color online) Relationship between shear stress and shear strain γ_{ZY} . (a) Macroscopic shear stress is estimated by using the average shear stress τ_{ZY} in regions including the grain boundary: $-30 \leq Y \leq 50$ nm. (b) Local shear stress is estimated by using τ_{ZY} in the stress concentration region produced by the dislocation pileup: $0 \leq Y \leq 5$ nm and $-2.5 \leq Z \leq 2.5$ nm. “+” represents the local shear stress τ_{zByB} in the region of the five Burgers vectors in front of the extrinsic grain boundary dislocation in model 1.

therefore, τ_{ZY}^I increases linearly with γ_{ZY} , as shown in Fig. 6(a). In order to examine this effect in greater detail, we consider the local shear stress τ_{zByB}^{III} in the region of five Burgers vectors in front of the first dislocation absorbed in the grain boundary (region III) in models 1 and 1', as shown in Fig. 6(b). Here, τ_{zByB}^{III} is estimated for the material coordinate system in grain B. In the linear dislocation theory, the stress τ_1 at the head of the pileup is n times the applied stress τ : $\tau_1 = n\tau$.²¹ In model 1', the local stress τ_{zByB}^{III} increases linearly with γ_{ZY} , as shown in Fig. 6(b); this is because the number of dislocations in the pileup is only 1 for a large value of γ_{ZY} . On the other hand, in model 1, the number of dislocations in the pileup increases with γ_{ZY} ; hence, τ_{zByB}^{III} increases nonlinearly. For the shear strain $\gamma_{ZY}=0.020$ and 0.022, the number of dislocations in the pileup is 3 in model 1 and 1 in model 1'. Therefore, the stress increment between $\gamma_{ZY}=0.020$ and 0.022 in model 1, $\Delta\tau_{zByB}$, can be estimated to

be three times larger than that in model 1'. The ratio of the stress increments in model 1 to those in model 1' in this study can be calculated as $(\Delta\tau_{zByB}^{III,1'} / \Delta\tau_{ZY}^{I,1'}) / (\Delta\tau_{zByB}^{III,1} / \Delta\tau_{ZY}^{I,1})$; its value is approximately 3.8. Therefore, these results of the atomistic simulations are in relatively good agreement with those of the linear dislocation theory for a small-angle grain boundary. Consequently, the transmission of the plastic deformation in model 1 occurs under a lower macroscopic shear stress, τ_{ZY}^I , than that of model 1' due to the dislocation pileup. This result is strongly related to the grain-size dependence of the strength in polycrystalline metals.

D. Force on the outgoing edge dislocation

In this section, the critical glide force f_c on the edge dislocation for it to eject from the tilt grain boundaries in models 1 and 2 is estimated by the following three methods. In the first method, the force f_c^{QC} is directly calculated by using the stress field near the dislocation that will be ejected in the QC simulations. In the second method, the critical force f_c^{dis} is evaluated by using the dislocation theory to consider it as the resultant of the force due to dislocations in the pileup and that due to the applied stress. The tilt grain boundaries in models 1 and 2 are completely expressed by the dislocations as shown in Figs. 3(a) and 3(b); therefore, in the third method, the critical force f_c^{GB} on the dislocation in a finite array of edge dislocations for it to eject from the array is estimated by the dislocation theory. We also discuss the expression capacity of the dislocation theory in comparison to the critical force f_c obtained by different methods in order to represent the structure of dense dislocations in the nanometer-scale range, e.g., the tilt grain boundary.

First, f_c^{QC} is evaluated as the force due to the average shear stress τ_{zByB}^{II} just before the dislocation ejection. τ_{zByB}^{II} is the microscopic shear stress estimated for the material coordinate system of grain B in region II. τ_{zByB}^{II} is 697 and 811 MPa when $\gamma_{ZY}=0.022$ in model 1 and $\gamma_{ZY}=0.032$ in model 2, respectively. Thus $f_{c,1}^{QC}$ in model 1 and $f_{c,2}^{QC}$ in model 2 can be obtained as follows:

$$f_{c,1}^{QC} = 0.199 \text{ N/m}, \quad f_{c,2}^{QC} = 0.232 \text{ N/m}.$$

Here, the ratio of $f_{c,1}^{QC}$ to $f_{c,2}^{QC}$ — $f_{c,1}^{QC}/f_{c,2}^{QC}$ —is approximately 1.17.

Next, f_c^{dis} is calculated as the resultant of the force f^{pil} due to the dislocation pileup and the force f^{AP} due to the applied stress. In dislocation theory, the interaction force on two edge dislocations on the same slip plane with parallel Burgers vectors \mathbf{b} can be expressed as $\mu b^2 / 2\pi(1-\nu)x$.²¹ Here, μ is the shear modulus; ν , Poisson's ratio; and x , the spacing between two dislocations. One dislocation lies in the grain boundary and the other lies in the pileup. The following material parameters are adopted for aluminum: $\mu=30$ GPa, $\nu=0.3$, and $b=0.286$ nm. Three and five dislocations are piled up when $\gamma_{ZY}=0.022$ in model 1 and $\gamma_{ZY}=0.032$ in model 2; in addition, the spacing x is 3.6, 9.5, and 19.9 nm in model 1, and 3.1, 7.9, 13.3, 20.2, and 27.9 nm in model 2, respectively. Thus, the resolved forces f_1^{pil} and f_2^{pil} along the slip direction in grain B are estimated as 0.237 N/m in model 1

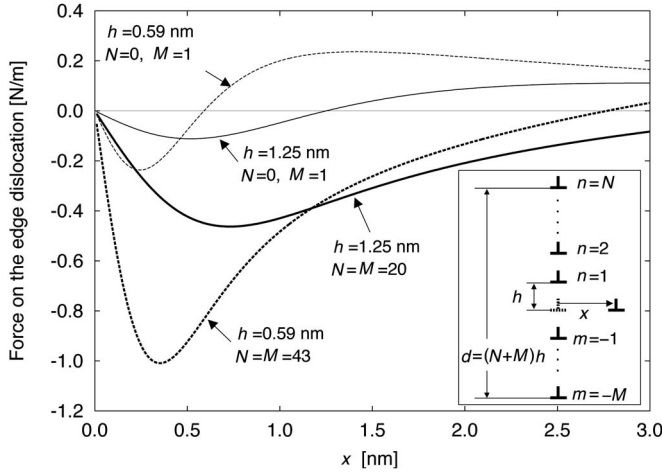


FIG. 7. Force on the middle edge dislocation in a finite array of edge dislocations. Thick lines represent the force in the finite array and the thin lines represent the interaction force between the parallel dislocations with parallel Burgers vectors.

and 0.297 N/m in model 2, respectively. On the other hand, the force f^{AP} due to the applied stress is calculated by the following equation:²¹

$$f_k = -\epsilon_{ijk}\xi_i\sigma_{jl}b_l. \quad (2)$$

Here, ξ , σ , and b are the unit vector of the dislocation line sense, the stress tensor on the glide plane, and the Burgers vector of the dislocation, respectively. The slip system of the outgoing edge dislocation from the grain boundary in models 1 and 2 is the same; therefore, $\xi=(1,0,0)$ and $b=a/\sqrt{2}(0,\cos\theta,-\sin\theta)$. θ is the misorientation angle of the grain boundary. The macroscopic shear stress τ_{ZY}^I just before the dislocation ejection, as shown in Fig. 6(a), is adopted as σ ; $\tau_{ZY}^I=247$ MPa when $\gamma_{ZY}=0.022$ in model 1 and $\tau_{ZY}^I=358$ MPa when $\gamma_{ZY}=0.032$ in model 2. Then, f^{AP} can be obtained as follows: $f_1^{\text{AP}}=0.064$ N/m in model 1 and $f_2^{\text{AP}}=0.053$ N/m in model 2. As a result, we can obtain the resultant f_c^{dis} in model 1 and model 2 as follows.

$$f_{c,1}^{\text{dis}}=0.301 \text{ N/m}, \quad f_{c,2}^{\text{dis}}=0.350 \text{ N/m}.$$

Although f_c^{dis} has a larger value than f_c^{QC} , it is found that the ratio $f_{c,2}^{\text{dis}}/f_{c,1}^{\text{dis}}$ is approximately 1.16 and is almost equivalent to the corresponding ratio for f_c^{QC} . Consequently, the glide force f_c^{QC} on the dislocation just before its ejection from the small-angle tilt grain boundary can be estimated as the force f_c^{dis} due to the dislocation pileup. Moreover, the applied stress estimated by using the dislocation theory and the critical force f_c exhibits a dependence on the grain boundary structure.

When the grain boundary structures in models 1 and 2 are regarded as a finite array of edge dislocations at regular intervals h , as shown in Fig. 7, the force on the middle edge dislocation in this finite array can be obtained according to dislocation theory by the following equation:³⁴

$$f_c^{\text{GB}} = \frac{\mu b^2}{2\pi(1-\nu)} 2 \sum_{n=1}^N \frac{x(x^2 - n^2 h^2)}{(x^2 + n^2 h^2)^2} \quad (3)$$

when $N=M$ in Fig. 7. Here, we do not consider the effect of the secondary IGBDs. As shown in Table I, $h=1.25$ nm for model 1 and $h=0.59$ nm for model 2. Assuming that the total length of the array of dislocations d is the Z -directional length of the simulation cell, $N=M=20$ for model 1 and $N=M=43$ for model 2. Figure 7 shows the force on the middle dislocations obtained by Eq. (3), and the force f_c^{GB} required to eject the middle dislocation from the grain boundary can be estimated as follows:

$$f_{c,1}^{\text{GB}}=0.463 \text{ N/m}, \quad f_{c,2}^{\text{GB}}=1.010 \text{ N/m}.$$

The values of f_c^{GB} are considerably larger than those of f_c^{QC} and f_c^{dis} , and the ratio $f_{c,2}^{\text{GB}}/f_{c,1}^{\text{GB}}$ is evaluated to be approximately 2.18. Hence, f_c^{GB} exhibits greater sensitivity to GBD density than the others. One of the causes of this discrepancy could be the effect of the dislocation core. A recently molecular dynamics simulation has revealed that the effect of dislocation core on the strain field appears when the crystal radius is smaller than 2 nm for aluminum.³⁵ In the tilt grain boundary obtained in these simulations, h is smaller than 2 nm for both models; hence, the structure of the dislocation core cannot be ignored at the boundaries. Consequently, it could be difficult to represent the actual elastic field created by the dense array of edge dislocations, e.g., small-angle tilt grain boundary, by using the dislocation theory without considering the dislocation core effect.

E. Accommodation mechanisms of extrinsic dislocations in tile grain boundaries

In order to elucidate the accommodation of EGBDs in the grain boundaries, Figs. 8–11 show a series of atomic configurations in the vicinity of the grain boundaries where the incoming dislocations are absorbed. We have only shown atoms that belong to the two atomic planes of $\{112\}$ along the X direction in the initial configuration. The colors used to represent the atoms are the same as those used in Fig. 4. The solid lines represent the Burgers circuits and slip plane of the incoming dislocations. In model 1, one vacancy and one primary IGBD are found in the Burgers circuit, as shown in Fig. 8. If one atom is located at the vacant site, one primary IGBD is introduced in the Burgers circuit, as shown in Fig. 4(a). No secondary IGBD is observed near the slip plane; hence, the grain boundary around the slip plane can be considered to be symmetrical. In model 2, as shown in Fig. 9(a), three primary IGBDs and one secondary IGBD are found in the Burgers circuit. Hence, the effect of the secondary IGBD on the accommodation of EGBDs can be investigated by comparing the results of these two models.

When γ_{ZY} reaches 0.012 in model 1, the incoming dislocation is absorbed in the site between the vacancy and IGBD A_{1-1}^I as the EGBD A_{1-1}^E , as shown in Fig. 8(b). Subsequent dislocations from the crack tip pile up behind A_{1-1}^E with an increase in γ_{ZY} , as shown in Fig. 5. Finally, A_{1-1}^E is ejected from the grain boundary when $\gamma_{ZY}=0.024$ and the next incoming dislocation is absorbed as A_{1-2}^E at the same site, as

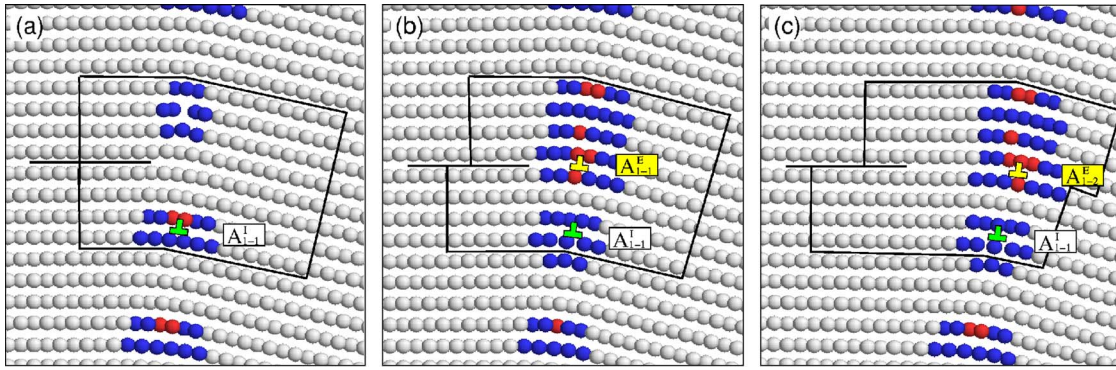


FIG. 8. (Color online) Atomic configurations of the tilt grain boundary in model 1 under shear deformation: γ_{ZY} = (a) 0.002, (b) 0.012, and (c) 0.024.

shown in Fig. 8(c). Consequently, the grain boundary can accommodate only one EGBD on the slip plane of the incoming dislocations.

In the equilibrium state in model 2, as shown in Fig. 9(a), IGBD A_{2-2}^I already exists on the slip plane of the incoming dislocation; therefore, it can be easily estimated that the first incoming dislocation will pile up behind A_{2-2}^I , as in the case of model 1. However, the first incoming dislocation does not pile up but is absorbed by the grain boundary as A_{2-1}^E , as shown in Fig. 9(b). This is due to the sliding of the secondary IGBD B_{2-1}^I along the grain boundary and the ejection of the atomic group, which corresponds to the magnitude of the Burgers vector of the incoming edge dislocation in the red (dark gray) box, from its atomic plane. Consequently, dislocations A_{2-2}^I , A_{2-3}^I , and A_{2-1}^E change their atomic planes; the dislocation climb-up and climb-down occur without the diffusion process. Furthermore, the symmetrical part of the grain boundary composed of A_{2-2}^I and A_{2-3}^I migrates to the left due to the sliding of B_{2-1}^I ; this can be considered as a DSC dislocation. As γ_{ZY} increases, the incoming dislocations pile up behind B_{2-1}^I . When γ_{ZY} reaches 0.028, B_{2-1}^I slides once again along the direction of the arrow, as shown in Fig. 9(b), and simultaneously, the second incoming dislocation is absorbed as A_{2-2}^E with a climb-up due to the sliding of B_{2-1}^I . There is no secondary IGBD in the upper region of the slip plane, as shown in Fig. 9(c); therefore, no accommodation of the EGBDs occurs in the grain boundary and the incoming

dislocations pile up behind A_{2-1}^E . Finally, A_{2-1}^E is ejected from the grain boundary by the dislocation pileup when γ_{ZY} reaches 0.034. It is noteworthy that the secondary IGBD, B_{2-1}^I , does not slide along under the macroscopic shear stress τ_{ZY} of 200–400 MPa in this study. Hence, the stress-assisted sliding along the grain boundary plane of the secondary IGBD with the absorption of the incoming dislocations could strongly affect the accommodation of EGBDs.

Next, we investigate models 3 and 4 with high-angle grain boundaries: these models cannot completely express the structure by dislocation arrays. In model 3, as shown in Figs. 4(c) and 10(a), the grain boundary structure comprises the periodic structure of $\Sigma 11$ and disorders. When the first incoming dislocation enters the disordered part of the grain boundary, as shown in Fig. 10(b), the geometrical misfit due to the incoming dislocation can be accommodated in the local region by the dislocation sliding of B_{3-1}^I and the rotation of atomic groups in the boxes. The second incoming dislocation is also accommodated by the local rotation of the atomic groups as shown in Fig. 10(c), when $\gamma_{ZY}=0.026$. Consequently, in the case of model 3, the geometrical misfits due to the EGBDs are accommodated not only by the sliding of the secondary IGBD but also by the local rotation of the atomic groups in the disordered region where the change in the free atomic volume occurs more easily than in the region composed of the edge dislocations. In the case of model 4, the grain boundary plane of grain B is the stable $\{111\}$ atomic plane. Hence, no significant accommodation of the

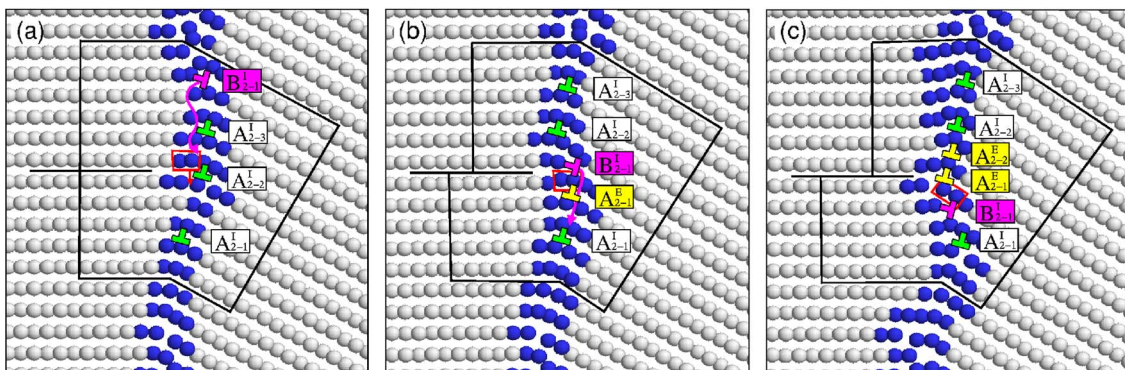


FIG. 9. (Color online) Atomic configurations of the tilt grain boundary in model 2 under shear deformation: γ_{ZY} = (a) 0.002, (b) 0.012, and (c) 0.028. The distributions of τ_{ZY} in the vicinity of the grain boundaries of (a) and (b) after the removal of γ_{ZY} are shown in Fig. 4.

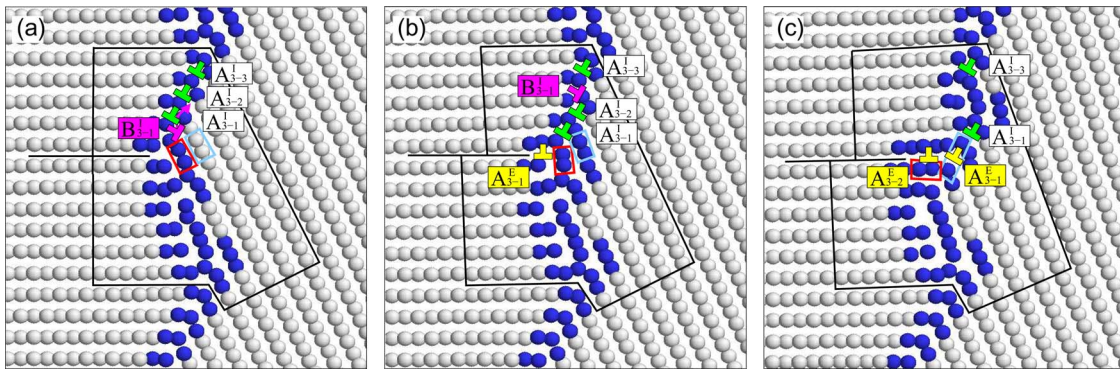


FIG. 10. (Color online) Atomic configurations of the tilt grain boundary in model 3 under shear deformation: γ_{ZY} = (a) 0.002, (b) 0.012, and (c) 0.026.

misfit in the local region along the grain boundary can be observed by tracking the atomic groups represented by the solid boxes. Further, it can be observed that the structure of the grain boundary becomes more disordered due to the absorption of the incoming dislocations, as shown in Fig. 11. The grain boundary sliding can be clearly observed because the grain boundary plane in model 4 is not wavy but straight. Consequently, it can be found that the accommodation mechanism of EGBDs strongly depends on the local grain boundary structure and the arrangements of GBs.

IV. DISCUSSION

Although the slopes of the plots of τ_{ZY}^{II} against γ_{ZY} are the same for each model before γ_{ZY} reaches 0.010, the increments in τ_{ZY}^{II} between 0.010 and 0.012 differ, as shown in Fig. 6(b)—288, 311, 338, and 223 MPa for models 1, 2, 3, and 4, respectively. The stress increment due to the EGBDs is influenced by their accommodation mechanism. However, it should be noted that the rate of increment of τ_{ZY}^{II} from the first to second dislocation absorption in each model does not show a remarkable dependence on the grain boundary structure. The rate, in fact, is governed by the elastic interactions between dislocations. Here, we consider a situation where the dislocation pileup occurs in one grain and the neighboring grain contains a Frank-Read (FR) source²¹ near the grain boundary between these two grains. The critical stress τ_c^{FR}

for the FR source to be active can be obtained as $\mu b/l$. l is the length of the segment of the dislocation whose ends are pinned. If the critical stress τ_c to eject a dislocation from the grain boundary is assumed to be approximately 800 MPa, as obtained in this study, the minimum l_c to operate the FR source under the same stress is approximately 10 nm. In the case where the neighboring grain contains an FR source with l greater than l_c , the transmission of plastic deformation occurs by the activation of the FR source due to the dislocation pileup without the emission of a dislocation from the grain boundary. Hence, it can be considered that the number of dislocations in the pileup is primarily related to the grain-size dependence of the material length in coarse grained metals. The mechanism of the Hall-Petch relationship can be well described by the pileup model in dislocation theory. On the other hand, in the case where l is shorter than l_c , the situation could intensity since with the grain size decreasing to nanometer order, plastic deformation is transmitted by the ejection of a dislocation from the grain boundary. The importance of this phenomenon is that the critical stress τ_c fundamentally shows a dependence on the grain boundary structure, and its value cannot be estimated simply by the dislocation theory. As a result, in nanocrystalline metals, the effect of the grain boundary characteristics on the macroscopic mechanical properties should not be ignored, and it can be confirmed that atomic simulations play an important role in elucidating the mechanical properties of such materials.

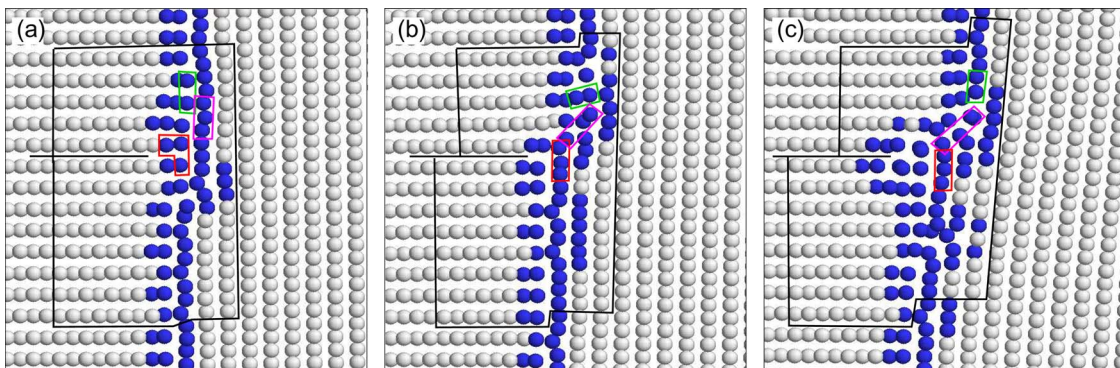


FIG. 11. (Color online) Atomic configurations of the tilt grain boundary in model 4 under shear deformation: γ_{ZY} = (a) 0.002, (b) 0.012, and (c) 0.028.

The analysis models used in this study do not possess grain boundary triple junctions. A triple junction could act as the source of grain boundary dislocation with the same Burgers vector as that of the secondary IGBD. If the triple junction exists near the upper part of the incoming slip plane in model 2, as shown in Fig. 9(c), and the grain boundary dislocations are generated from the triple junction, the grain boundary could accommodate more EGBDs without using diffusion processes. Since the volume fraction of the triple junction increases as the grain size reaches the nanometer range, the absorption power of the incoming dislocations presumably exhibits grain-size dependence. This grain-size dependence could be one of the reasons for the distinctive mechanical properties of nanocrystalline metals.^{4,5} Furthermore, the grain boundary edge dislocations are densely arranged along the grain boundary by the accommodation of EGBDs, as shown in Fig. 9(c). Therefore, the local misorientation angle increases. This rearrangement of the grain boundary dislocations implies that grain rotation occurs easily in nanocrystalline metals.^{36,37}

V. CONCLUSIONS

The interactions between the $\langle 112 \rangle$ asymmetrical tilt grain boundaries and edge dislocations are efficiently simulated by using the QC method, and the accommodation mechanisms of extrinsic dislocations in the grain boundaries are discussed. Four types of equilibrium grain boundaries with different misorientation angles are considered. The results obtained in this study are follows. (i) The rate of stress concentration increment due to the dislocation pileup does not show a remarkable dependence on the grain boundary structure when the accommodation of EGBDs occurs in a localized region. (ii) The critical force on a dislocation for it to eject from the small-angle tilt grain boundary is examined by using atomic models and dislocation theory, and its dependence on the grain boundary structure is also discussed.

(iii) The accommodation mechanism of the extrinsic dislocations strongly depends on the local grain boundary structures. In particular, the rearrangement of the grain boundary dislocations due to the sliding of the secondary IGBDs along the grain boundary plane in the local region where the absorption of the extrinsic dislocation occurs could be one of the characteristic accommodation processes of the asymmetrical tilt grain boundary. Based on the above-mentioned results, the effects of the interaction between dislocations and grain boundaries on the mechanical properties of coarse-grained metals with dislocation sources in their grain and on nanocrystalline metals without these sources in their grain are also considered.

Although static simulations at 0 K are adopted in this study, the motions of a dislocation and grain boundary exhibit dynamic and thermal effects, e.g., the influence of the velocity of dislocation on its stacking fault width,³⁸ and the transition of grain boundary deformation modes at various temperatures.³⁹ Hence, it is very important to investigate the thermal effect on the mechanism of interaction between dislocations and grain boundaries. Moreover, it would also be interesting to investigate the influence of the stacking fault energy on the interaction mechanism. However, these effects are beyond the framework of this paper and will be studied in future work.

ACKNOWLEDGMENTS

The authors would like to thank K. W. Jacobsen, J. Schiøtz, and J. J. Mortensen for fruitful discussions. T.S. acknowledges the support from the Ministry of Education, Science, Sports and Culture, Grant-in-Aid for Young Scientists (B), No. 16760063. This study was supported in part by a Grant-in-Aid for Scientific Research from the Ministry of Education, Culture, Sports, Science and Technology (MEXT), Japan on Priority Areas "Giant Straining Process for Advanced Materials Containing Ultra-High Density Lattice Defects."

¹E. O. Hall, Proc. Phys. Soc. London, Sect. B **64**, 747 (1951).

²N. J. Petch, J. Iron Steel Inst., London **174**, 25 (1953).

³J. W. Wyrzykowski and M. W. Grabski, Philos. Mag. A **53**, 505 (1986).

⁴Y. M. Wang, E. Ma, R. Z. Valiev, and Y. T. Zhu, Adv. Mater. (Weinheim, Ger.) **16**, 328 (2004).

⁵X. Huang, N. Hansen, and N. Tsuji, Science **312**, 249 (2006).

⁶H. Gleiter, Acta Mater. **48**, 1 (2000).

⁷L. Priester, Interface Sci. **4**, 205 (1997).

⁸A. A. Nazarov, Interface Sci. **8**, 71 (2000).

⁹J. P. Couzinié, B. Décamps, and L. Priester, Int. J. Plast. **21**, 759 (2005).

¹⁰P. H. Pumphrey and H. Gleiter, Philos. Mag. **30**, 593 (1974).

¹¹R. Z. Valiev, V. Y. Gertsman, and O. A. Kaibyshev, Phys. Status Solidi A **78**, 177 (1983).

¹²A. A. Nazarov, A. E. Romanov, and R. Z. Valiev, Scr. Metall. Mater. **24**, 1929 (1990).

¹³J. Schiøtz and K. W. Jacobsen, Science **301**, 1357 (2003).

¹⁴V. Yamakov, D. Wolf, S. R. Phillpot, and H. Gleiter, Acta Mater. **51**, 1971 (2003).

¹⁵H. Van Swygenhoven, P. M. Derlet, and A. G. Froseth, Nat. Mater. **3**, 399 (2004).

¹⁶T. Shimokawa, T. Kinari, S. Shintaku, A. Nakatani, and H. Kitagawa, Modell. Simul. Mater. Sci. Eng. **13**, 1217 (2005).

¹⁷Y. W. Zhang and T. C. Wang, Modell. Simul. Mater. Sci. Eng. **4**, 231 (1996).

¹⁸D. Saraev and S. Schmauder, Phys. Status Solidi B **240**, 81 (2003).

¹⁹Z.-H. Jin, P. Gumbsch, E. Ma, K. Albe, K. Lu, H. Hahn, and H. Gleiter, Scr. Mater. **54**, 1163 (2006).

²⁰H. Jang and D. Farkas, Mater. Lett. **61**, 868 (2006).

²¹J. P. Hirth and J. Lothe, *Theory of Dislocations*, 2nd ed. (McGraw-Hill, New York, 1968).

²²E. B. Tadmor, R. Phillips, and M. Ortiz, Langmuir **12**, 4529

- (1996).
- ²³V. B. Shenoy, R. Miller, E. B. Tadmor, R. Phillips, and M. Ortiz, Phys. Rev. Lett. **80**, 742 (1998).
- ²⁴R. Miller, M. Ortiz, R. Phillips, V. Shenoy, and E. B. Tadmor, Eng. Fract. Mech. **61**, 427 (1998).
- ²⁵S. Hai and E. B. Tadmor, Acta Mater. **51**, 117 (2003).
- ²⁶V. B. Shenoy, R. Miller, E. B. Tadmor, D. Rodney, R. Phillips, and M. Ortiz, J. Mech. Phys. Solids **47**, 611 (1999).
- ²⁷T. Shimokawa, J. J. Mortensen, J. Schiøtz, and K. W. Jacobsen, Phys. Rev. B **69**, 214104 (2004).
- ²⁸Y. Mishin, D. Farkas, M. J. Mehl, and D. A. Papaconstantopoulos, Phys. Rev. B **59**, 3393 (1999).
- ²⁹J. Dana Honeycutt and H. C. Andersen, J. Phys. Chem. **91**, 4950 (1987).
- ³⁰W. T. Read and W. Shockley, Phys. Rev. **78**, 275 (1950).
- ³¹J. Schiøtz, T. Vegge, F. D. Di Tolla, and K. W. Jacobsen, Phys. Rev. B **60**, 11971 (1999).
- ³²J. Y. Huang, Y. T. Zhu, H. Jiang, and T. C. Lowe, Acta Mater. **49**, 1497 (2001).
- ³³H. Grimmer, W. Bollmann, and D. H. Warrington, Acta Crystallogr., Sect. A: Cryst. Phys., Diffr., Theor. Gen. Crystallogr. **30**, 197 (1974).
- ³⁴V. Bata and E. V. Pereloma, Acta Mater. **52**, 657 (2004).
- ³⁵C. H. Henager, Jr. and R. G. Hoagland, Scr. Mater. **50**, 1091 (2004).
- ³⁶T. Shimokawa, A. Nakatani, and H. Kitagawa, Phys. Rev. B **71**, 224110 (2005).
- ³⁷M. Y. Gutkin, I. A. Ovid'ko, and N. V. Skiba, Acta Mater. **51**, 4059 (2003).
- ³⁸J. Weertman, in *Mathematical Theory of Dislocations*, edited by T. Mura (American Society of Mechanical Engineering, New York, 1968).
- ³⁹J. W. Cahn, Y. Mishin, and A. Suzuki, Acta Mater. **54**, 4953 (2006).